Studies of the pedestal structure and inter-ELM pedestal evolution in JET with the ITER-like wall

Original
Studies of the pedestal structure and inter-ELM pedestal evolution in JET with the ITER-like wall / Maggi, C.F., Frassinetti, L., Horvath, L., Lunniss, A., Saarelma, S., Wilson, H., Flanagan, J., Leyland, M., Lupelli, I., Pamela, S., Urano, H., Garzotti, L., Lerche, E., Nunes, I., Rimini, F., Subba, F.. - In: NUCLEAR FUSION. - ISSN 0029-5515. - 57:11(2017). [10.1088/1741-4326/aa7e8e]

Availability:
This version is available at: 11583/2986895 since: 2024-03-12T16:22:37Z

Publisher:
IOP PUBLISHING LTD

Published
DOI:10.1088/1741-4326/aa7e8e

IAEA nuclear fusion

PAPER

Studies of the pedestal structure and inter-ELM pedestal evolution in JET with the ITER-like wall

To cite this article: C.F. Maggi *et al* 2017 *Nucl. Fusion* **57** 116012

IOP Publishing | International Atomic Energy Agency Nuclear Fusion

Nucl. Fusion **57** (2017) 116012 (15pp) https://doi.org/10.1088/1741-4326/aa7e8e

Studies of the pedestal structure and inter-ELM pedestal evolution in JET with the ITER-like wall

C.F. Maggi[1], L. Frassinetti[2], L. Horvath[3], A. Lunniss[3], S. Saarelma[1], H. Wilson[3], J. Flanagan[1], M. Leyland[3], I. Lupelli[1], S. Pamela[1], H. Urano[4], L. Garzotti[1], E. Lerche[1], I. Nunes[5], F. Rimini[1] and JET Contributors[a]

EUROfusion Consortium, JET, Culham Science Centre, Abingdon OX14 3DB, United Kingdom
[1] CCFE, Culham Science Centre, Abingdon OX14 3DB, United Kingdom
[2] Association VR, Fusion Plasma Physics, KTH, SE-10044 Stockholm, Sweden
[3] Department of Physics, York Plasma Institute, University of York, York YO10 5DD, United Kingdom
[4] National Institutes for QST, Naka 311-0193, Japan
[5] Associação IST, Instituto Superior Técnico, Av Rovisco Pais, 1049-001 Lisbon, Portugal

E-mail: Costanza.Maggi@ukaea.uk

Received 16 December 2016, revised 22 June 2017
Accepted for publication 10 July 2017
Published 3 August 2017

Abstract

The pedestal structure of type I ELMy H-modes has been analysed for JET with the ITER-like Wall (JET-ILW). The electron pressure pedestal width is independent of ρ^* and increases proportionally to $\sqrt{\beta_{\text{pol,PED}}}$. Additional broadening of the width is observed, at constant $\beta_{\text{pol, PED}}$, with increasing ν^* and/or neutral gas injection and the contribution of atomic physics effects in setting the pedestal width cannot as yet be ruled out. Neutral penetration alone does not determine the shape of the edge density profile in JET-ILW. The ratio of electron density to electron temperature scale lengths in the edge transport barrier region, η_e, is of order 2–3 within experimental uncertainties. Existing understanding, represented in the stationary linear peeling–ballooning mode stability and the EPED pedestal structure models, is extended to the dynamic evolution between ELM crashes in JET-ILW, in order to test the assumptions underlying these two models. The inter-ELM temporal evolution of the pedestal structure in JET-ILW is not unique, but depends on discharge conditions, such as heating power and gas injection levels. The strong reduction in $p_{\text{e,PED}}$ with increasing D_2 gas injection at high power is primarily due to clamping of ∇T_e half way through the ELM cycle and is suggestive of turbulence limiting the T_e pedestal growth. The inter-ELM pedestal pressure evolution in JET-ILW is consistent with the EPED model assumptions at low gas rates and only at low beta at high gas rates. At higher beta and high gas rate the inter-ELM pedestal pressure evolution is qualitatively consistent with the kinetic ballooning mode (KBM) constraint but the peeling–ballooning (*P–B*) constraint is not satisfied and the ELM trigger mechanism remains as yet unexplained.

Keywords: H-mode, pedestal structure, inter-ELM pedestal evolution, JET-ILW

(Some figures may appear in colour only in the online journal)

---

[a] See the author list of 'Overview of the JET results in support to ITER' by X. Litaudon *et al* in *Nuclear Fusion* Special issue: Overview and summary reports from the *26th Fusion Energy Conference (Kyoto, Japan, 17–22 October 2016)*.

1. Introduction

The understanding of the structure of the pedestal region that sustains H-mode plasmas is crucial for the prediction of the performance of next step tokamaks. The strength of the edge transport barrier provides the boundary conditions that determine the turbulent transport levels in the plasma core.

Recent pedestal studies in JET have focussed on the characterization of the H-mode pedestal structure with the ITER-like Be/W wall (JET-ILW), in which the pedestal evolution is limited by type I edge localized modes (ELMs). While previous work concentrated on pedestal confinement and assessment of the MHD stability, this work turns to the question of inter-ELM transport, which determines the temporal evolution of the pedestal parameters between subsequent ELM crashes. This paper focuses primarily on the analysis of the temporal evolution of the pedestal parameters during the ELM cycle and on the characterization of the experimental evidence from JET-ILW, as a first step towards understanding inter-ELM transport and how the ELM trigger is reached under varying plasma conditions. The second stage of the analysis should involve linear and non-linear edge gyrokinetic calculations to qualify and quantify the inter-ELM transport levels measured experimentally in JET-ILW.

The primary dataset analysed in this paper, unless otherwise stated, is composed of systematic power scans at 1.4 MA/1.7 T at 3 levels of D_2 gas rate injection: 3×10^{21} e s^{-1} (‘low gas‘), 8×10^{21} e s^{-1} (‘medium gas’) and 1.8×10^{22} e s^{-1} (‘high gas’) [1]. Recent experiments have extended this dataset to lower power to map empirically the type I/type III ELM boundary and connect to $P_{\mathrm{L-H}}$, the H-mode threshold power. In JET-ILW the type I/type III ELM boundary lies just above $P_{\mathrm{L-H}}$ and is therefore observed at reduced pedestal temperature, $T_{\mathrm{e,PED}}$, compared to JET with the Carbon wall (JET-C). As previously reported, $P_{\mathrm{L-H}}$ is lower in JET-ILW in the high density branch [2]. The dataset at 1.4 MA/1.7 T connects to the hybrid scenario at low gas rate/high beta (with beta the normalized plasma pressure) and to the high plasma current (I_{P}) baseline scenario (albeit at lower $I_{\mathrm{P}}/B_{\mathrm{T}}$, with B_{T} the toroidal magnetic field) at high gas rate/medium-low beta, as shown e.g. in [3]. One of the strengths of this dataset of power scans is that, due to the relatively low $I_{\mathrm{P}}/B_{\mathrm{T}}$ for JET, the auxiliary heating power could be increased significantly above $P_{\mathrm{L-H}}$. As a result, a variation in normalized beta, $\beta_{\mathrm{N}} = \beta\ a\ B_{\mathrm{T}}/I_{\mathrm{P}}$ (with a the plasma minor radius), of a factor of two is obtained in the type I ELMy regime, enabling the study of inter-ELM pedestal evolution with respect to plasma beta. As variations in power and gas rate are decoupled in these experiments, the inter-ELM pedestal evolution can also be investigated in relation to varying gas injection levels. A connection with high I_{P}, $q_{95} = 3$ JET-ILW baseline scenario pedestals is achieved by comparing the inter-ELM pedestal evolution at 1.4 MA and 3.0 MA.

The paper is organized as follows: section 2 describes the experimental characterization of the pedestal structure in JET-ILW; section 3 reviews the scaling of the pedestal width in JET-ILW, as measured in various dimensional and dimensionless experiments in type I ELMy H-modes, and compares the measured pedestal density width to the neutral penetration model [4]; in section 4 the temporal evolution of JET-ILW pedestal parameters during the ELM cycle is presented and discussed in the framework of the predictive pedestal model EPED [5]; conclusions and implications of this work are drawn in section 5.

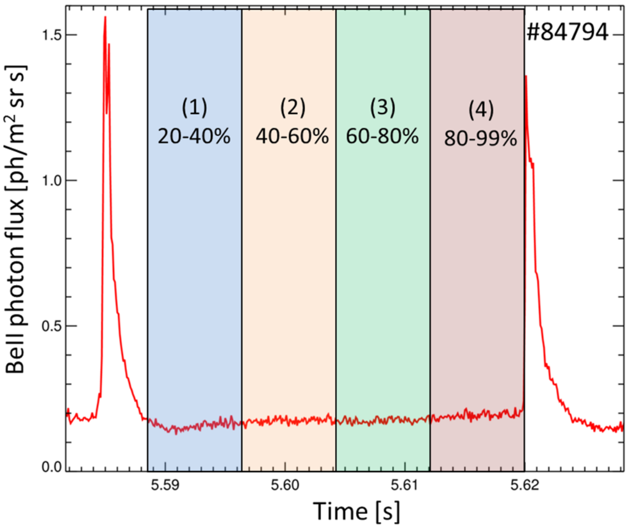

Figure 1. The ELM cycle is normalized to a relative time scale from 0 to 100% and divided into equal, 20% long intervals. The first interval, 0–20%, is omitted from the analysis as it is often affected by the ELM crash phase.

2. Characterization of the pedestal structure

The electron pedestal structure is characterized in geometrical form by the height, gradient and width of the pedestal region. In this work it is measured primarily using high resolution thomson scattering (HRTS) [6], with a sampling frequency of 20 Hz. The HRTS data are also validated against high time resolution electron cyclotron emission (ECE) [7] data (0.4 ms) for the T_{e} profiles measurements, in particular for the inter-ELM temporal evolution studies of section 4, and against Li-beam [8] (~15 ms) and reflectometry [9] data (sampling rate >15 μs) for the n_{e} profiles, when available. The ion pressure p_{i} cannot be characterized to this detail in terms of temporal resolution, so we focus on the electron pedestal pressure in this work. Typically, $T_{\mathrm{i}} = T_{\mathrm{e}}$ at the plasma edge in the dataset analysed in this paper.

For a given discharge, the HRTS profiles collected from a steady time window are ELM-syncronized to form a composite profile. The ELM cycle is normalized to a relative time scale and divided into 20% long intervals, as shown in figure 1, to improve data statistics. The parameters for density (n_{e}) and temperature (T_{e}) are evaluated by means of modified hyperbolic tangent function (mtanh) fits [10] to the respective profiles. The first ELM interval, 0–20%, is ignored, as it is often affected by the ELM crash phase. The pre-ELM quantities are those relating to the 80–99% ELM interval and are used for the pedestal width scaling studies in section 3. In the pedestal region the spatial sampling of the HRTS diagnostic is ~8 mm and the FWHM is ~1 cm [11], which is smaller than

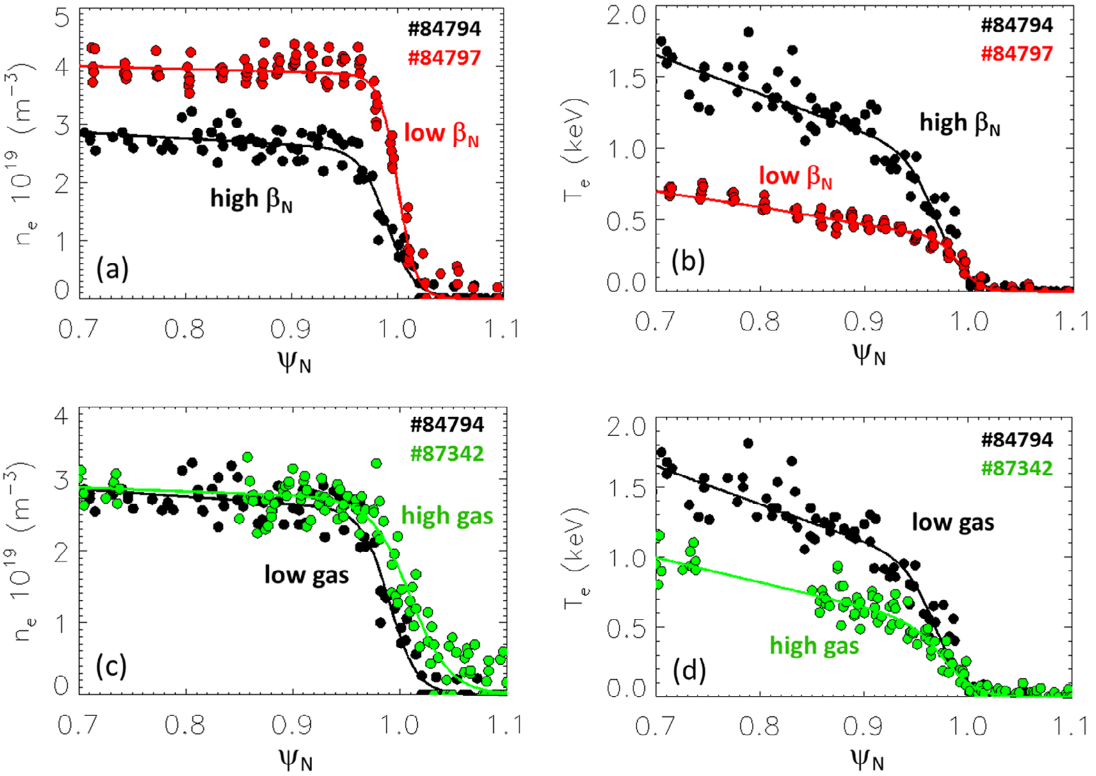

Figure 2. Representative examples of HRTS n_e and T_e profiles and corresponding mtanh fits (solid lines) for the comparison of low versus high beta at low gas rate (*a*) and (*b*) and for the comparison at low versus high gas rate at highest input power (15 MW of NBI heating) in the power and gas scans (*c*) and (*d*). All profiles correspond to the 80–99% interval of the ELM cycle.

the minimum pedestal width observed on JET [12], but larger than the inter-chord spacing. Therefore, the instrument function is numerically calculated and convolved with the mtanh function when fitting the profiles for an accurate estimate of the pedestal width [11, 12]. In addition, the spatial resolution in the pedestal changes from shot to shot as it is related to the number of HRTS profiles included in the composite profile. As described in [11, 12], all profiles in the given interval of the ELM cycle are used in the fits. To compensate for the fact that the last closed flux surface (LCFS) position might slightly vary from profile to profile, the selected HRTS profiles are aligned by applying a radial shift. The applied radial shift corresponds to the change, from profile to profile, in the intersection between the LCFS and the HRTS lines of sight. The fits to the HRTS profiles are performed in real space and then mapped on the normalized poloidal flux ψ. We also note that due to the uncertainty in the radial position of the profiles, caused mainly by the uncertainty in the EFIT equilibrium reconstruction, the profiles (see, e.g. figure 2) are shifted radially according to a two-point model for the power balance at the magnetic separatrix [13] so that $T_{e,sep} \sim 100\,\text{eV}$ (with $T_{e,sep}$ the separatrix electron temperature). An equal radial shift is applied to the density profile. The uncertainties in the mtanh fit parameters represent the errors on the pedestal parameters. Examples of HRTS n_e and T_e profiles, and their corresponding mtanh fits, are shown in figure 2 for the comparison of low versus high β_N at low gas rate (figures 2(*a*) and (*b*)) and for the comparison at low versus high gas rate at highest input power (15 MW of NBI heating) in the scans (figures 2(*c*) and (*d*)). In figure 2 all profiles correspond to the 80–99% interval of the ELM cycle.

In this paper we adopt the definitions commonly used in literature of $p_{e,PED} = k\ T_{e,PED} \times n_{e,PED}$ for the pedestal pressure height and of $\Delta p_e(\psi) = ½(\Delta T_e(\psi) + \Delta n_e(\psi))$ for the pedestal pressure width. This facilitates comparison of new analysis from this work with published material, which adopted these definitions. We note, however, that $T_{e,PED}$ and $n_{e,PED}$ are not found at the same radial location, with the n_e profile typically radially outwards of the T_e profile. For instance, for the power and gas scans dataset the relative shift between n_e and T_e profiles is observed to increase with power and from low to medium gas rate at a given power. Changes in the relative n_e–T_e profiles shift have been shown to correlate to changes in pedestal stability, both in JET [14] and in ASDEX-Upgrade [15], but this aspect is not a topic of this study. For the purpose of this work it is important to note that the different radial location of the n_e and T_e pedestals has a potential implication on the definition of the pedestal pressure parameters. We have therefore also derived $p_{e,PED}$ and $\Delta p_e(\psi)$ directly from modified hyperbolic tangent fits (*mtanh*) to the HRTS electron pressure profile data (without deconvolution of the HRTS instrument function). In figure 3 we compare the two definitions of pedestal pressure height and width for discharge #87342 ($\beta_N = 2$, high D_2 gas rate) for the four intervals of the ELM cycle. A systematic quantitative difference is observed between the two definitions, with *mtanh* fits to the pressure profile data yielding narrower widths and marginally lower $p_{e,PED}$ values, although their time evolution during the

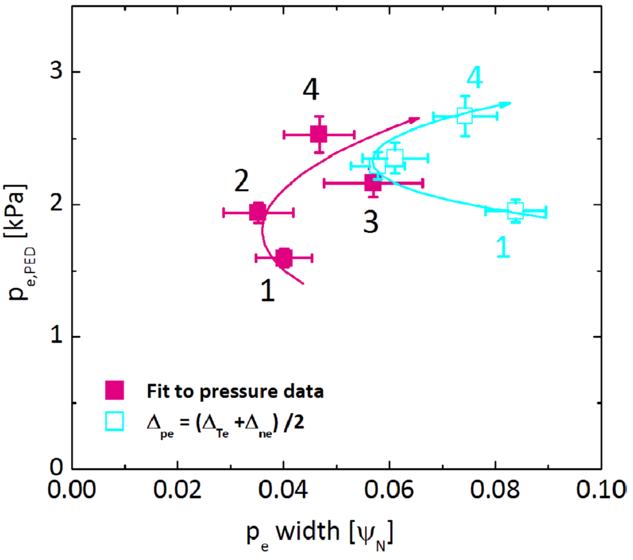

Figure 3. Comparison of definitions of $p_{\rm e,PED}$ and $\Delta p_{\rm e}$ for the 4 intervals of the ELM cycle for discharge #87342: in magenta, solid squares the two parameters extracted from mtanh fits of $p_{\rm e}$ profiles; in cyan open squares the two parameters obtained from separate mtanh fits of $n_{\rm e}$ and $T_{\rm e}$ profiles and $p_{\rm e,PED} = k\,T_{\rm e,PED} \times n_{\rm e,PED}$, $\Delta p_{\rm e} = ½(\Delta T_{\rm e} + \Delta n_{\rm e})$. The solid lines through the data are merely to guide the eye.

ELM cycle is qualitatively similar in the two cases. Typically, $\Delta p_{\rm e}(\psi)$ values derived from *mtanh* fits to the HRTS electron pressure profile have larger error bars than $\Delta p_{\rm e}(\psi) = ½(\Delta T_{\rm e}(\psi) + \Delta n_{\rm e}(\psi))$. Therefore, any subtle difference in inter-ELM evolution of the pressure width between the two derivations cannot be extracted unambiguously within experimental uncertainties. This provides additional motivation for the choice of $p_{\rm e,PED}$ and $\Delta p_{\rm e}(\psi)$ definitions adopted in this work.

Edge pressure gradient and edge current density are the two key parameters that determine the pedestal stability. The current density in the pedestal is dominated by the bootstrap current, $j_{\rm BS}$, primarily driven by the edge pressure gradient, but also strongly influenced by the edge collisionality, ν^*. ν^* is the normalized collisionality defined as the ion–electron collision rate normalized to the thermal ion bounce frequency $\nu^* = 6.91 \times 10^{-18} R q_{95} Z_{\rm eff} \ln\Lambda / \left(\varepsilon^{3/2} T_{\rm e}^2\right)$ [16, 17] (with R the major radius, q the safety factor, $Z_{\rm eff}$ the effective charge, ε the inverse aspect ratio, $T_{\rm e}$ the electron temperature and $\ln\Lambda$ the Coulomb logarithm). The edge $j_{\rm BS}$ profile is calculated with the local neoclassical transport code NEO [18, 19], which solves the drift-kinetic equation with a full linearized Fokker–Planck collision operator including all inter-species collisions. This allows for a more accurate estimate of $j_{\rm BS}$ than using the Sauter formula [16, 17], especially in JET pedestals at high ν^*, where $j_{\rm BS}$ (Sauter) has been shown to overestimate $j_{\rm BS}$ (NEO) by up to a factor of two [1]. The input to NEO are the EFIT plasma equilibrium, the electron kinetic profiles ($T_{\rm i}$ is assumed equal to $T_{\rm e}$) and the line averaged $Z_{\rm eff}$ (measured from visible Bremsstrahlung) to evaluate the ion density, with Be as the intrinsic impurity. Analysis of the inter-ELM evolution of the edge bootstrap current for JET-ILW pedestals under varying operational conditions is reported elsewhere [20].

3. Pedestal width scaling

Dimensionless scans in normalized poloidal ion Larmor radius ρ^* ($\rho^* = \sqrt{(2Am_{\rm p}T_{\rm i})}/(eBa)$, with A the mass number, $m_{\rm p}$ the proton mass, $T_{\rm i}$ the ion temperature, e the electron charge, B the poloidal magnetic field and a the minor radius), with constant q_{95}, ν^* and thermal β ($\beta_{\rm th} = (p_{\rm e} + p_{\rm i})/B^2/\mu_0$), have confirmed the absence of a sizeable scaling of $\Delta p_{\rm e}(\psi)$ with ρ^* in JET-ILW [21], consistently with earlier findings in JET-C/DIII-D ρ^* scan experiments [22] and in JT-60U [23]. Moreover, also the normalized pressure gradient does not depend on ρ^*, within the uncertainty in the data [21]. These findings project favourably to ITER operation, at least as far as pedestal pressure width and normalized gradient are concerned.

Similarly to what is observed in several tokamaks, including JET-C, in JET-ILW the pre-ELM electron pedestal pressure width increases with pedestal poloidal beta, $\beta_{\rm pol,PED} = p_{\rm PED}/(\langle B_{\rm p}\rangle^2/2\mu_0)$, in ψ space, proportionally to $\sqrt{\beta_{\rm pol,PED}}$ [1], as assumed in the EPED model [5]. $p_{\rm PED}$ is the total pedestal top pressure, $p_{\rm i,PED} + p_{\rm e,PED}$, and $\langle B_{\rm p}\rangle$ the average poloidal magnetic field at the pedestal top. The pedestal broadening in ψ space can be associated with the increase in Shafranov shift, via a non linear feedback loop involving core-edge coupling, which stabilizes the ballooning modes [24, 25].

On the other hand, high plasma triangularity (δ) pedestals at high D_2 injection rates—a necessary condition in JET-ILW to enable steady H-mode conditions compatible with core W control over longer time scales—are not fully consistent with the EPED model assumptions. In these plasmas the pedestal widens at constant $\beta_{\rm pol,PED}$ with increasing pedestal top collisionality, $\nu^*_{\rm PED}$, thus deviating from the kinetic ballooning modes (KBM)-based dependence of the pedestal width posited in the model [26]. In recent dimensionless H-mode experiments at low δ, where $\nu^*_{\rm PED}$ was varied by a factor of 5 at constant q_{95}, normalized ion Larmor radius ρ^* and normalized thermal β, $\Delta p_{\rm e}(\psi)$ broadens at constant $\beta_{\rm pol,PED}$ with increasing $\nu^*_{\rm PED}$. Regression to the data shows $\Delta p_{\rm e}(\psi) \sim (\beta_{\rm pol,PED})^{0.5}(\nu^*_{\rm PED})^{0.26}$ [27]. In the dimensional power and gas scan experiments, which resulted in a factor of 10 variation in $\nu^*_{\rm PED}$, $\Delta p_{\rm e}(\psi)$ broadens with increasing gas rate at constant $\beta_{\rm pol,PED}$, as shown in figure 4 and as was discussed in [1], in analogy to the findings of [26]. However, in contrast to the results of the ν^* scan of [27], the normalized width $\Delta_{\rm p}(\psi)/\sqrt{\beta_{\rm pol,ped}}$ is constant with $\nu^*_{\rm PED}$, but is larger at higher D_2 gas rates at a given value of $\nu^*_{\rm PED}$ (e.g. see figure 8(*b*) of [1]). At the highest gas rate injection in the scan, $\Delta_{\rm p}(\psi)/\sqrt{\beta_{\rm pol,ped}}$ possibly even decreases with $\nu^*_{\rm PED}$ rather than increasing with it. Therefore, the combined results of the dimensional and dimensionless experiments do not necessarily indicate a dependence of $\Delta p_{\rm e}(\psi)$ on ν^*, in addition to that on $\sqrt{\beta_{\rm pol,PED}}$. Rather, they may be indicative of an additional dependence of the pedestal width on parameters either directly or indirectly connected with the D neutral content in the plasma, implying that atomic physics effects could also contribute in setting the pedestal width.

In the dimensional power and gas scans the variation in $\beta_{\rm pol,PED}$ is caused by variations in both injected neutral beam (NB) power, $\rm P_{NBI}$, and gas rate. Both $\Delta n_{\rm e}(\psi)$ and $\Delta T_{\rm e}(\psi)$ broaden with gas rate at constant $\beta_{\rm pol,PED}$, in analogy with the

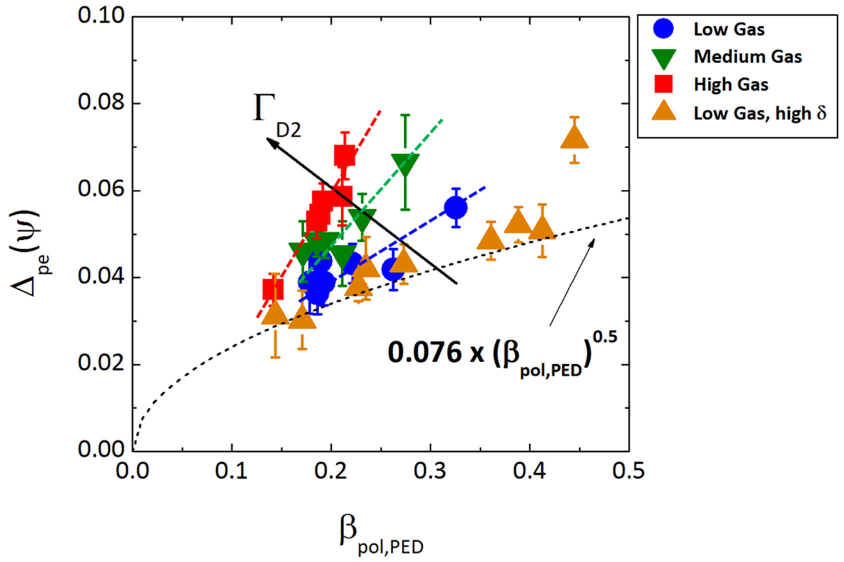

Figure 4. Pre-ELM pedestal p_e width as a function of $\beta_{\text{pol, PED}}$ for the 1.4 MA/1.7 T power scans at low δ with increasing D_2 gas injection (blue circles: low gas rate = 3×10^{21} e s^{-1}; green down-triangles: medium gas rate = 8×10^{21} e s^{-1}; red squares: high gas rate = 1.6×10^{22} e s^{-1}) and at high δ (orange up-triangles: low gas rate = 3×10^{21} e s^{-1} from experiments of [1, 3]).

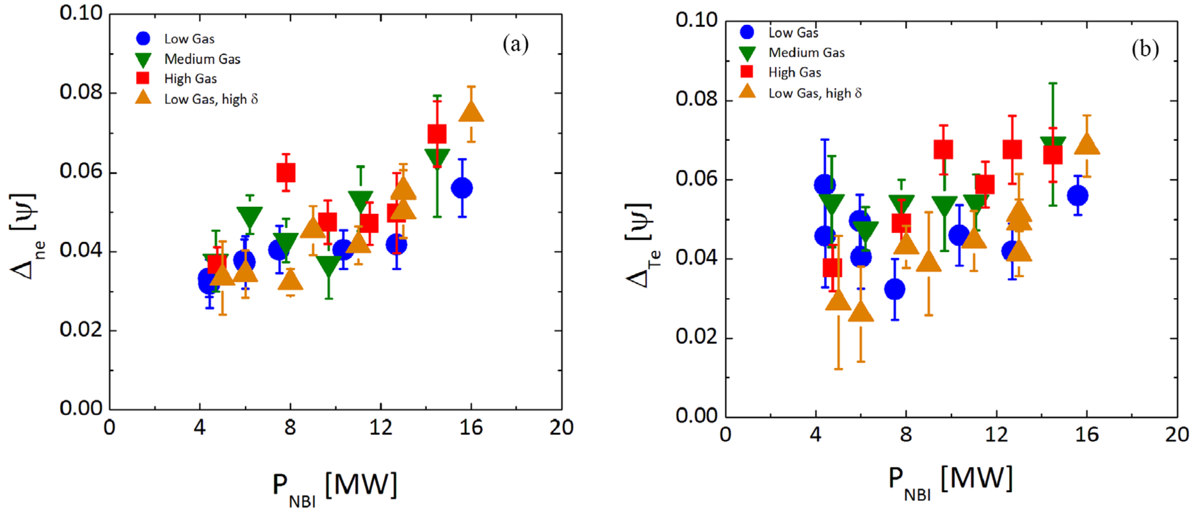

Figure 5. Pre-ELM pedestal widths for n_e (*a*) and T_e (*b*) versus injected NB power (same notations as for figure 4). While Δn_e broadens with NBI power, but does not vary significantly with gas rate (within error bars) at any P_{NBI} value, the variation of ΔT_e is more complex: for the low δ discharges (blue, green and red symbols), ΔT_e broadens with gas rate at constant P_{NBI} at intermediate power values, but is similar at low and high gas rates above 14 MW, and ΔT_e broadens linearly with P_{NBI} only for the low gas, high δ dataset (orange triangles).

broadening of $\Delta p_e(\psi)$ shown in figure 4. On the other hand, while Δn_e broadens with NBI power, but does not vary significantly with gas rate (within error bars) at any P_{NBI} value, except possibly at the highest power of the scan (figure 5(*a*)), the variation of ΔT_e with power is more complex (figure 5(*b*)): for the low triangularity (δ) discharges, ΔT_e broadens with gas rate at constant P_{NBI} at intermediate power values, but is similar at low and high gas rates above 14 MW, and ΔT_e broadens linearly with P_{NBI} only for the low gas, high δ dataset (orange triangles in figure 5). This shows that while Δn_e is largely unaffected by variations in D_2 gas rate, ΔT_e is affected by them at high input power above $P_{\text{L–H}}$ ($P_{\text{NBI}} > 14$ MW in figure 5), where a systematic broadening of ΔT_e with gas rate is observed.

The neutral penetration model for the density width [4] assumes that the shape of the n_e profile is determined by edge fuelling and constant diffusion, with the width of the edge transport barrier being proportional to the neutral penetration length. In its simplest formulation, if charge exchange processes are neglected, the model predicts $\Delta n_e \sim 1/n_{e,\text{PED}}$, which can quickly be tested against the experimental pedestal widths to check whether the model captures the main trend in the data. Comparison to JET-ILW n_e widths indicates that for some datasets Δn_e is broadly consistent with the neutral penetration model predictions, as shown in figure 6(*a*) for a low δ dataset of type I ELMy H-modes with $I_P = 1.4$–4.0 MA and $B_T = 1.7$–3.7 T. Note that it's charge exchange (CX) processes that allow neutral penetration inside the LCFS at high

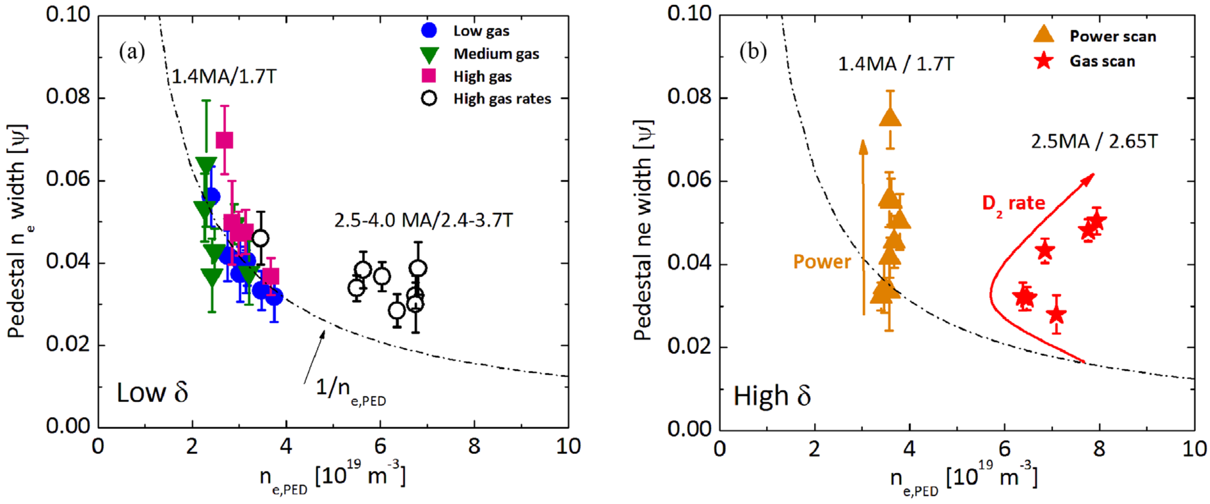

Figure 6. Comparison of JET-ILW pedestal n_e widths with the assumptions of the neutral penetration model, $\Delta n_e \sim 1/n_{e,PED}$: (*a*) low δ type I ELMy H-modes at 1.4 MA/1.7 T (power and gas scans) and at higher I_P/B_T and D_2 rates (open black circles); (*b*) high δ power scan at 1.4 MA/1.7 T, low D_2 gas rate (orange triangles) and D_2 gas rate at constant power at 2.5 MA/2.7 T (red stars).

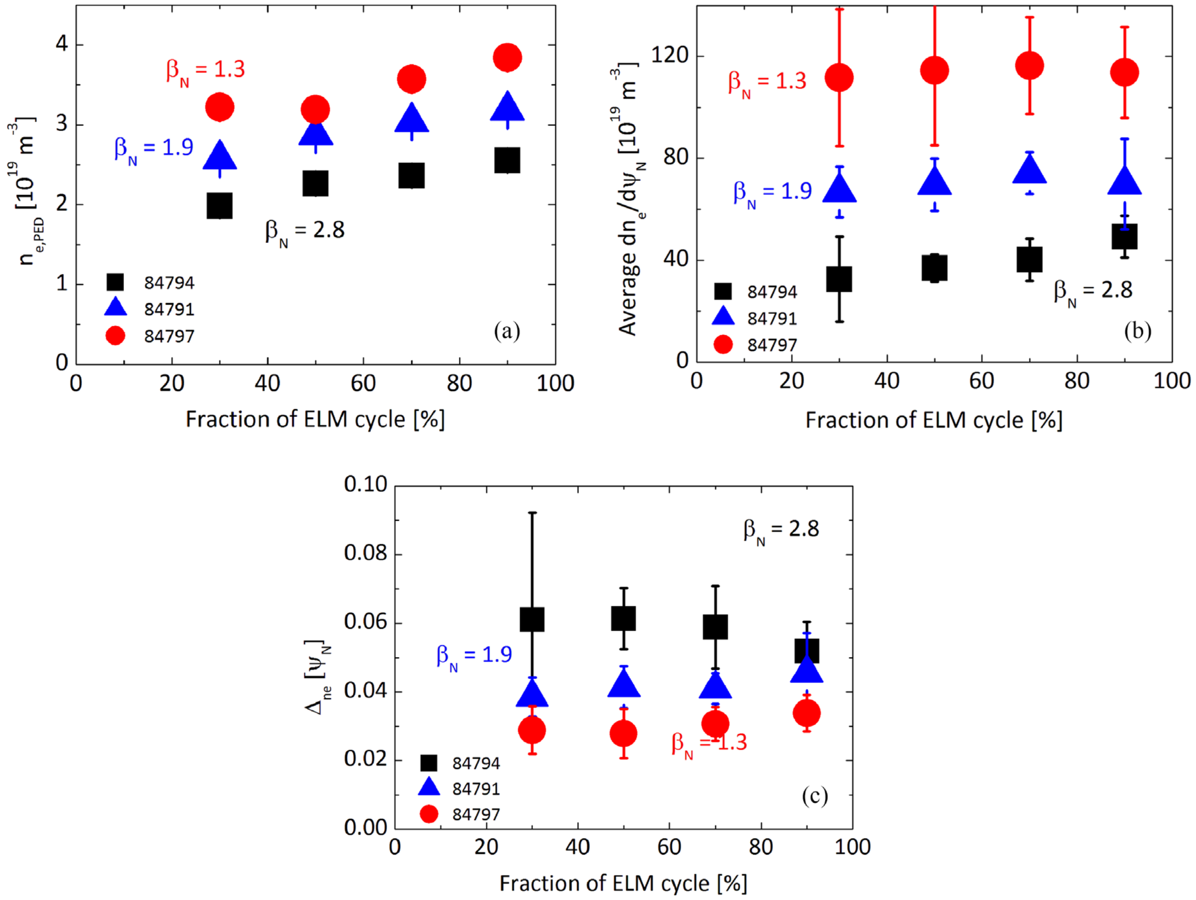

Figure 7. Pedestal n_e evolution during the type I ELM cycle of the 1.4 MA/1.7 T power scans at low D_2 gas injection: (*a*) $n_{e,PED}$, (*b*) average ∇n_e and (*c*) Δn_e as a function of normalized ELM fraction. Red circles = discharge at lowest β_N, black squares = discharge at highest β_N, blue triangles = discharge at an intermediate β_N value in the power scan.

pedestal density, therefore this effect needs to be taken into account for more quantitative comparisons. Saturation of the n_e width to a constant value at high $n_{e,PED}$ (figure 6(*a*)) may indeed indicate CX setting neutral penetration at high density. Figure 6(*b*) tests the neutral penetration model against two JET-ILW datasets at high δ. Both the power scan at 1.4 MA/1.7 T (orange triangles, from data in [1])—with Δn_e increasing at constant $n_{e,PED}$) and the D_2 gas scan at constant power at 2.5 MA/2.65 T (red stars, from data in [26]) deviate strongly from the simple approximation of the model. We note that it is not necessarily implied here that the reason for the discrepancy is ascribed to the difference in plasma triangularity in the two

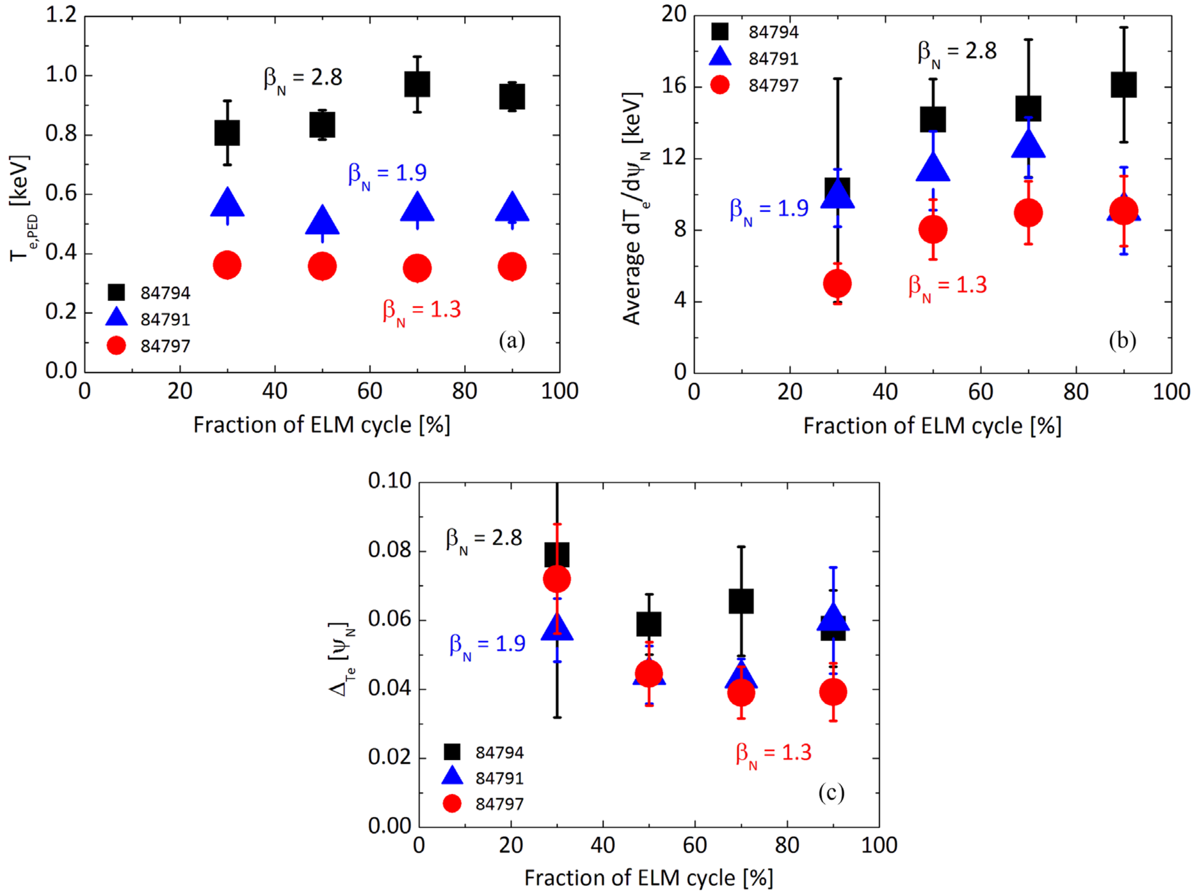

Figure 8. Pedestal T_e evolution during the type I ELM cycle of the 1.4 MA/1.7 T power scans at low D_2 gas injection: (*a*) $T_{e,PED}$, (*b*) average ∇T_e and (*c*) ΔT_e as a function of normalized ELM fraction. Red circles = discharge at lowest β_N, black squares = discharge at highest β_N, blue triangles = discharge at an intermediate β_N value in the power scan.

datasets, as this may be purely coincidental. The dashed black curves in figures 6(*a*) and (*b*) indicate a variation of $\Delta n_e \sim 1/n_{e,PED}$. The model is thus too simple and does not capture all the physics of the wider database. Another dataset which is at odds with the neutral penetration model assumptions is that of dimensionless ν^* scans discussed in [27], which exhibit substantial broadening of Δn_e at roughly constant $n_{e,PED}$. In summary, neutral penetration alone does not appear to set the n_e width in JET-ILW, but a combination of source and transport effects is likely to set the shape of the pedestal n_e profile in JET-ILW, as pointed out in an earlier analysis for AUG data [28]. It is possible that, depending on the discharge conditions, neutral penetration effects may become dominant compared to transport effects. One such example may be the n_e width variation in the datasets of figures 6(*a*) and (*b*) discussed above (although the underlying physics reason remains as yet unexplained). A physics model for the pedestal density that captures all conditions of the operating space is missing and is an important element for achieving full predictive capability of the pedestal height.

4. Pedestal evolution during the ELM cycle

Whereas MHD modelling can assess pedestal stability, it cannot describe the inter-ELM transport which drives the temporal evolution of the pedestal parameters between subsequent ELM crashes. The main aim of this work is to study the temporal evolution of the pedestal parameters during the ELM cycle and characterize the experimental evidence, as a first step towards understanding inter-ELM transport and how the ELM trigger is reached under varying plasma conditions in JET-ILW. In particular, in this work we study how the pre-ELM density, temperature and pressure are achieved as a function of heating power, D_2 gas injection rate and plasma current.

If KBM are assumed to control the pressure gradient evolution during the type I ELM cycle, as within the EPED model framework, the build-up of the pedestal should occur first with the pedestal pressure gradient growing unconstrained until the KBM boundary is reached, and subsequently with p_{PED} increasing through widening of the pedestal pressure width at fixed gradient (KBM constraint), until the Peeling–Ballooning modes (*P*–*B*) boundary is reached and the type-I ELM is triggered (*P*–*B* constraint). We note that a study of JET-C high δ H-modes had found, for low D_2 gas injection conditions, the pedestal height to increase due to steepening of the pressure gradient and narrowing of the pressure width during the inter-ELM pedestal recovery phase, in contrast to the pedestal gradient being limited by KBMs [29].

In this study we find that the inter-ELM pedestal evolution in JET-ILW doesn't follow only one dynamic pattern, but varies depending on plasma conditions, often in a complex fashion.

It is not always consistent with the assumptions underpinning the EPED model. We analyse separately the inter-ELM evolution of pedestal density and temperature, as they exhibit different dynamics, which may help identifying the nature of the turbulence driving the inter-ELM transport. In the next sections we first study the inter-ELM pedestal evolution as the heating power is varied in the power scans. H-modes at low D_2 gas injection (section 4.1) are distinguished from those at high gas injection (section 4.2), as their pedestal stability is different at higher beta values [1]. In section 4.3 the inter-ELM pedestal evolution in JET-ILW is studied with respect to variations in plasma current, from low $I_P = 1.4$ MA of the power and gas scans to $I_P = 3$ MA of recent, high performance baseline H-modes at $q_{95} = 3$ and $\beta_N \sim 2$. They provide a first insight on the comparison of inter-ELM transport in JET-ILW at high and low ρ^* values, respectively.

4.1. Inter-ELM pedestal evolution of power scan at low D_2 gas injection

The pre-ELM edge stability, calculated with HELENA/ELITE [30, 31], is consistent with the *P–B* model throughout the power scan [1, 3]: the EPED model *P–B* constraint is satisfied.

We examine first the inter-ELM evolution of the density and temperature pedestals separately and then the evolution of the pedestal pressure. Figure 7(*a*) shows that $n_{e,PED}$ decreases with power (or β_N), roughly by 30% overall, as the ELM frequency, f_{ELM}, increases with power (as shown in figure 6(*b*) of ref [1]). At any β_N value $n_{e,PED}$ grows monotonically during the ELM cycle. At the highest β_N achieved in the power scan, there is a trend for ∇n_e to steepen (figure 7(*b*)) and for Δn_e to narrow (figure 7(*c*)) until the ELM occurs, suggesting in this case qualitative consistency with the neutral penetration model [4], although the inter-ELM pedestal evolution at low and medium beta does not show this behaviour. The density gradient is significantly larger at low power than at high power.

$T_{e,PED}$ increases substantially as the net input power across the separatrix, P_{sep}, is increased from two times (#84797) to eight times (#84794) above P_{L-H}, but, unlike $n_{e,PED}$, it remains largely constant during the ELM cycle, except at the highest power ($\beta_N = 2.8$), where $T_{e,PED}$ grows until the last 30% of the ELM cycle and then flattens until the ELM crash (figure 8(*a*)). Here, P_{sep} is calculated as $P_{sep} = P_{loss} - P_{rad,bulk}$ (with the loss power $P_{loss} = P_{heat} - dW/dt$, $P_{rad,bulk}$ the power radiated inside the LCFS, P_{heat} the total heating power including Ohmic heating and dW/dt the rate of change of the plasma stored energy). At low and medium power levels, ∇T_e initially steepens and then saturates (figure 8(*b*)) while ΔT_e first narrows and then remains constant in the second half of the ELM cycle (figure 8(*c*)). At $\beta_N = 2.8$ $T_{e,PED}$ may be growing due to steepening of the gradient at constant width, although this cannot be firmly ascertained within the experimental uncertainties. The temperature width is broader and the gradient steeper at high power than at low power.

Figures 7 and 8 show that from the lowest to the highest power in the scan the pre-ELM average density gradient in the pedestal roughly halves and the average temperature gradient roughly doubles, consistent with doubling β_N. In terms of the ratio of density to temperature scale lengths in the edge transport barrier, $\eta_e = L_{n_e}/L_{T_e}$, it would be expected that η_e increases from the low power to the high power pedestal. An inspection of the pedestal gradients using η_e as metric allows for a direct investigation of the profiles, independently from any regularization introduced by the *mtanh* fit. In figure 9 the pre-ELM edge T_e and n_e profile data—from pedestal top to pedestal foot—are plotted against each other in a log–log scale and $\eta_e = d(\log T_e)/d(\log n_e)$. A linear fit to the data, including the uncertainties in the n_e and T_e data points, shows that $\eta_e \sim 2$ within uncertainties in both shots. Therefore HRTS data with higher temporal and spatial resolution are needed to enable an accurate quantitative discrimination of the variation in η_e from low to high power.

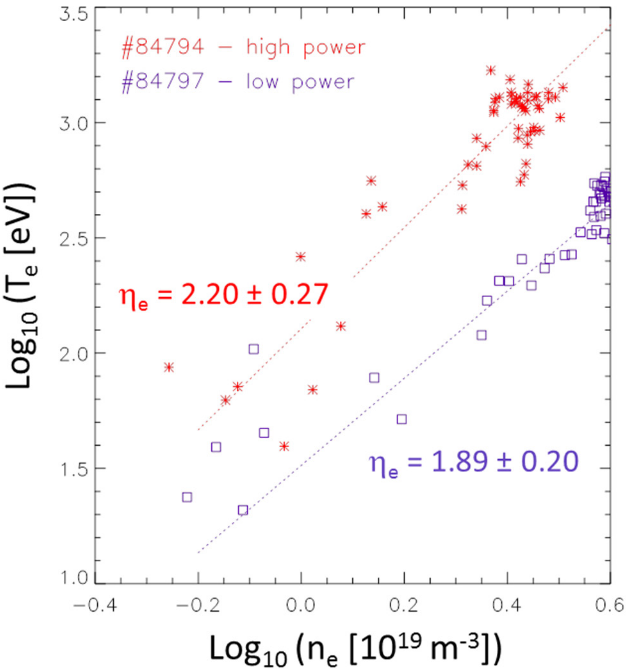

Figure 9. Log (T_e) versus log (n_e) in the pedestal region for the two H-mode discharges at 1.4 MA/1.7 T at low gas rate, low (purple) and high (red) power, indicating an increase in $\eta_e = d(\log T_e)/d(\log n_e)$ with power, due to an increase in ∇T_e and a reduction in ∇n_e. The lines are linear fits to the experimental HRTS data (pre-ELM values), taking into account the uncertainties in the T_e and n_e data.

As a result of the variations of $T_{e,PED}$ and $n_{e,PED}$ with power discussed above, $p_{e,PED}$ increases with power (figure 10(*a*)). $p_{e,PED}$ first grows due to steepening of the average gradient (figure 10(*b*)) and narrowing of the pressure width (figure 10(*c*)) and then in the latter part of the ELM cycle ∇p_e saturates and Δp_e remains roughly constant within error bars. This dynamics is qualitatively consistent with the presence of instabilities clamping the pressure gradient during the ELM cycle (i.e. qualitatively consistent with the KBM constraint) as posited in the EPED model. As the pedestal pressure evolution at low D_2 gas injection is consistent with the *P–B* constraint and qualitatively consistent with the KBM constraint, it could follow the EPED model assumptions.

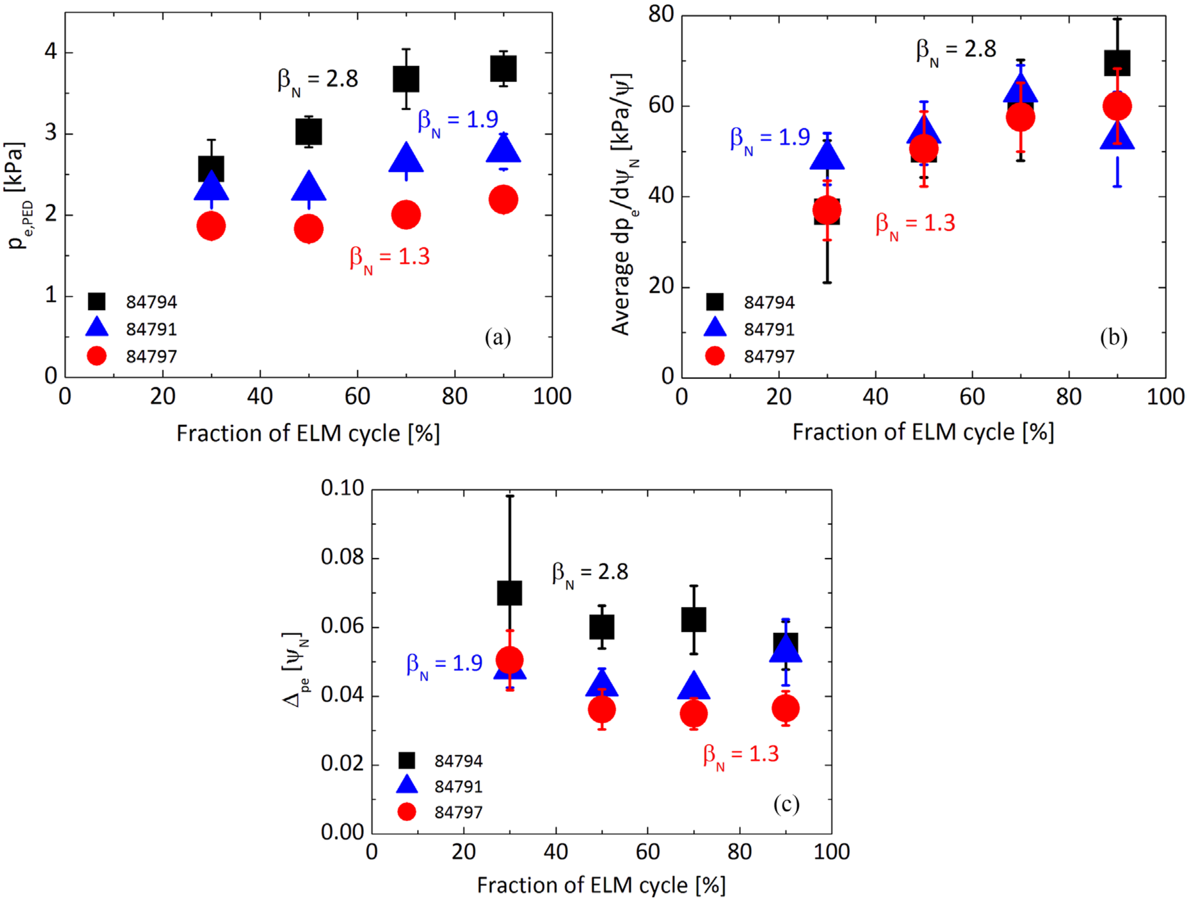

Figure 10. Pedestal p_e evolution during the type I ELM cycle for three H-modes of the 1.4 MA/1.7 T power scans at low D_2 gas injection: (*a*) $p_{e,PED}$, (*b*) average ∇p_e and (*c*) Δp_e as a function of normalized ELM fraction.

4.2. Inter-ELM pedestal evolution of power scan at high D_2 gas injection

At high gas rates, the pre-ELM edge stability is consistent with the ELMs being triggered by *P–B* modes at low β_N, but it predicts the pedestal to be deeply stable to *P–B* modes at high β_N [1]. Although the ELMs are empirically identified as being of type I with the power scan, they are different in character compared to type I ELMs at low gas rates [1]. This discrepancy between *P–B* model and experiment points to missing physics for the ELM instability onset. The EPED model *P–B* constraint is satisfied at low β_N, but is not satisfied at higher β_N.

As in the low gas case, $n_{e,PED}$ decreases with power (f_{ELM} increases) in all phases of the ELM cycle (from #87346 to #87342) and increases during the ELM cycle at all power levels (figure 11(*a*)), although more moderately than in the discharges at low gas injection, and flattens from 60% of the ELM cycle at low and medium β_N. After the initial build-up phase, there is a trend for the average density gradient to decreases before the ELM crash at high β_N and to flatten first and then increase at medium β_N (figure 11(*b*)). At the lowest beta the trend may be similar to that at $\beta_N = 2.0$, although the larger error bars do not exclude constancy of the average gradient during the ELM cycle. Δn_e increases/decreases towards the end of the ELM cycle at high/medium β_N (figure 11(*c*)), compensating somewhat for the decrease/increase of the gradient and at low β_N remains largely unvaried during the ELM cycle within error bars. As the D_2 gas rate increases at constant power, $T_{e,PED}$ is degraded compared to the low gas case, in particular at higher power (see figure 2(*d*)). At the highest beta achieved in the power scan at high gas rate ($\beta_N = 2$), and to within error bars, $T_{e,PED}$ saturates half way through the ELM cycle, due to clamping of ∇T_e (figure 12(*b*)) at constant width (figure 12(*c*)). Therefore, the reduction in $p_{e,PED}$ with increasing D_2 gas injection measured in JET-ILW at higher β_N, at constant net input power [1], is primarily due to the clamping of $T_{e,PED}$ half way through the ELM cycle and—in the last 20–30% of the ELM cycle—to flattening of the density gradient and widening of the density width. This is suggestive of turbulence limiting the T_e pedestal growth [32], while the n_e pedestal can still develop. In other words, the measurements suggest that the inter-ELM heat transport can be significant, especially at high power above $P_{L\text{–}H}$. Clamping of $T_{e,PED}$ and ∇T_e increases ν^* and reduces the pressure gradient, effects that both lead to a reduction in edge bootstrap current and concomitant decrease in edge stability. Therefore, these measurements indicate that avoiding saturation of the temperature gradient as the pedestal rebuilds in between ELM crashes is crucial to maximizing pedestal performance in JET-ILW. At low and medium β_N $T_{e,PED}$ hardly changes during the ELM cycle: at $\beta_N = 1.7$ this is due to clamping of ∇T_e at roughly constant width, whereas at $\beta_N = 1.2$ the average

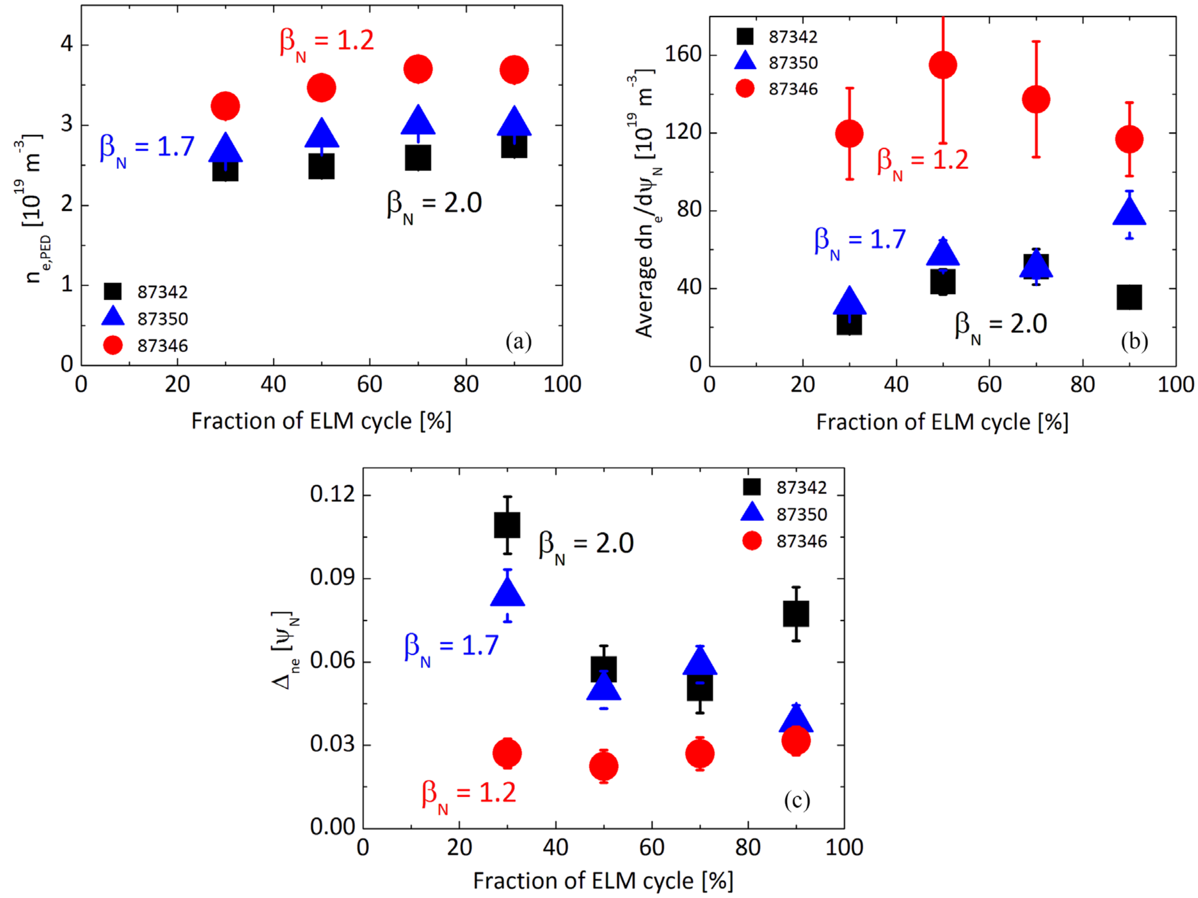

Figure 11. Pedestal n_e evolution during the type I ELM cycle of the 1.4 MA/1.7 T power scans at high D_2 gas injection: (*a*) $n_{e,PED}$, (*b*) average ∇n_e and (*c*) Δn_e as a function of normalized ELM fraction. Red circles = discharge at lowest β_N, black squares = discharge at highest β_N, blue triangles = discharge at an intermediate β_N value in the power scan.

gradient first steepens while the width narrows, followed by a drop in ∇T_e and broadening in ΔT_e in the last 30% of the ELM cycle.

Analysis of η_e values—in the pre-ELM phase—at low versus high gas rates for the two pedestals at the highest P_{sep} ~ 13 MW in the power scans yields $\eta_e = 2.2$ for pulse #84794 at low gas rate and $\eta_e = 3.7$ for pulse #87342 at high gas rate (figure 13), indicating an increase in η_e from low to high gas rate at high power. On the other hand, the larger scatter in the HRTS data for the pulse at high gas makes the evaluation of η_e for this shot more uncertain. As stated earlier, HRTS data with higher spatial and temporal resolution are needed to enable a more accurate quantitative discrimination of η_e in the variation from low to high gas at high input power. Ultimately, gyro-kinetic (GK) simulations of the experimental profiles should be carried out, which will hopefully indicate the nature of the underlying turbulence and help capturing the experimental transport levels.

We now turn to the analysis of the inter-ELM pedestal pressure evolution at high gas rate (figure 14). The pressure height increases during the ELM cycle (figure 14(*a*)), initially due to steepening of the gradient and narrowing of the width, followed by a reduction/saturation of average ∇p_e at low/high β_N and an increase in Δp_e at the end of the ELM cycle, while at $\beta_N = 1.7$ Δp_e narrows after the ELM crash, remains constant between 40 and 70% of the ELM interval and then narrows further in the last 30% of the ELM cycle (figures 14(*b*) and (*c*)). The pedestal pressure dynamical evolution at low and high β_N is qualitatively consistent with the KBM constraint. Therefore, the inter-ELM build-up of $p_{e,PED}$ at low β_N and high gas rate could be consistent with the EPED model assumptions, since both *P–B* and KBM constraints are satisfied. In contrast, at the highest β_N achieved at high gas rate, $\beta_N = 2$, the inter-ELM temporal evolution of the pedestal pressure is not consistent with the EPED model assumptions as the *P–B* constraint is not satisfied [1].

In the pedestals at high gas rate and higher β_N, where ∇T_e is clamped half way through the ELM cycle, other types of instabilities than KBMs could be responsible for limiting the growth of the pedestal height. As microtearing modes (MTMs) are driven by the electron temperature gradient, they exhibit the characteristics of a mode that clamps the T_e pedestal evolution, and could therefore be the dominant turbulence in the JET-ILW pedestal when the D_2 gas rate is progressively increased at given input power. Recent non-linear GENE simulations of a sample JET-ILW pedestal at high D_2 gas rate indicate that MTM and electron temperature gradient driven turbulence, together with neoclassical transport, is consistent with power balance across the pedestal, with KBMs largely insignificant over the edge transport barrier, except

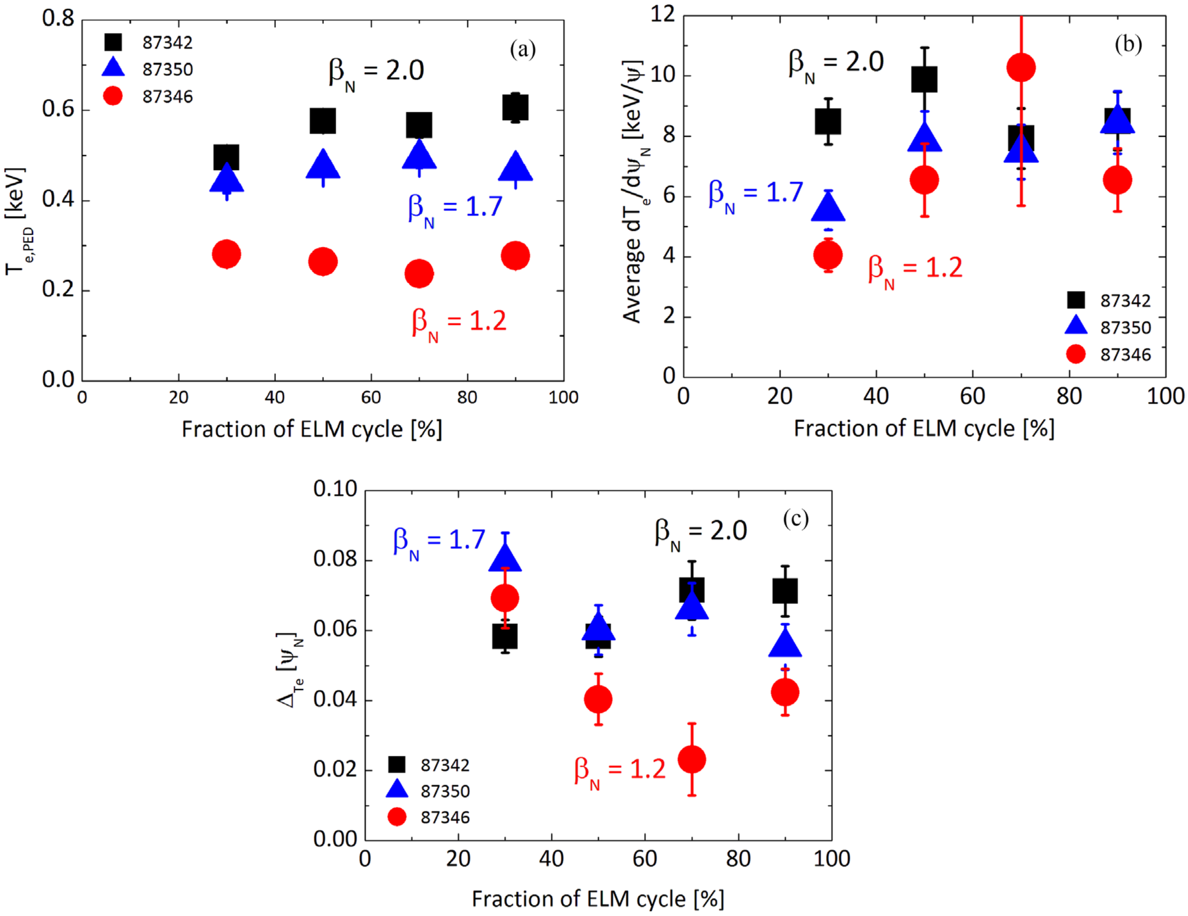

Figure 12. Pedestal T_e evolution during the type I ELM cycle of the 1.4 MA/1.7 T power scans at high D_2 gas injection: (*a*) $T_{e,PED}$, (*b*) average ∇T_e and (*c*) ΔT_e as a function of normalized ELM fraction.

very near the LCFS [32]. Non-linear GK analyses of the pedestals studied in this work are therefore required to answer these questions. In parallel, experimental identification of the nature of the turbulence driving the residual pedestal transport inter-ELM should also be pursued, for instance by comparing the pedestal gradient evolution to the fluctuation levels measured by reflectometry.

4.3. Inter-ELM pedestal evolution at low and high plasma current

Recently, good performance type I ELMy H-mode operation with $H_{98} = 1$ (with H_{98} the thermal energy confinement normalized to the confinement expected from the IPB98(y, 2) scaling [33]) and $\beta_N \geqslant 2$ has been achieved in JET-ILW in the high current baseline scenario at 3.0 MA/2.8 T ($q_{95} = 3$) at low plasma triangularity, with ~30 MW auxiliary heating. While the analysis of these experiments will be presented elsewhere, a representative discharge is selected for comparison with the low I_p discharges analysed in section 4.1. An overview of the main plasma parameters of the chosen low and high I_P H-modes is shown in table 1. All parameters are averaged in the steady time window Δt. Operation at high I_p leads to a substantial increase in pedestal electron pressure due to an increase in $n_{e,PED}$ (which roughly doubles with I_P), while $T_{e,PED}$ remains close to 1 keV in #92432, a value similar to that

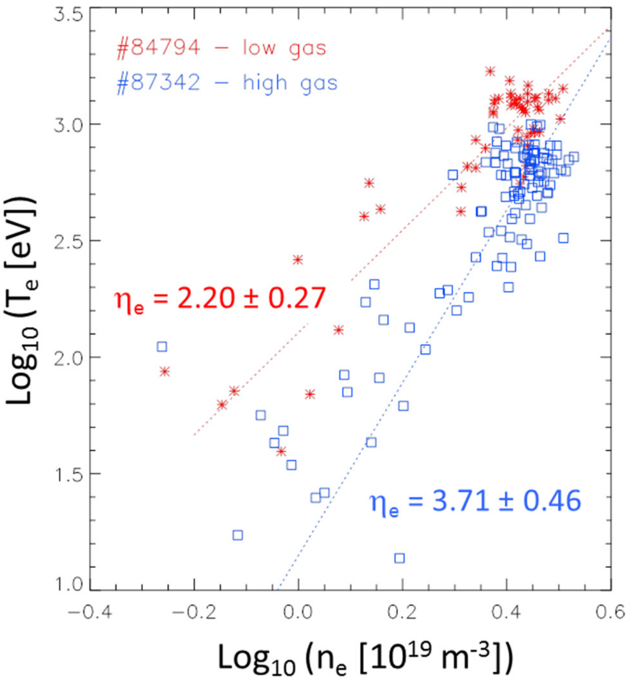

Figure 13. Log (T_e) versus log (n_e) in the pedestal region for the two H-mode discharges at 1.4 MA/1.7 T at similar P_{sep} ~ 13 MW, showing η_e = d (log T_e)/d (log n_e) at low (red) versus high (blue) D_2 gas rate. The lines are linear fits to the HRTS data (pre-ELM values), taking into account the uncertainties in the T_e and n_e data.

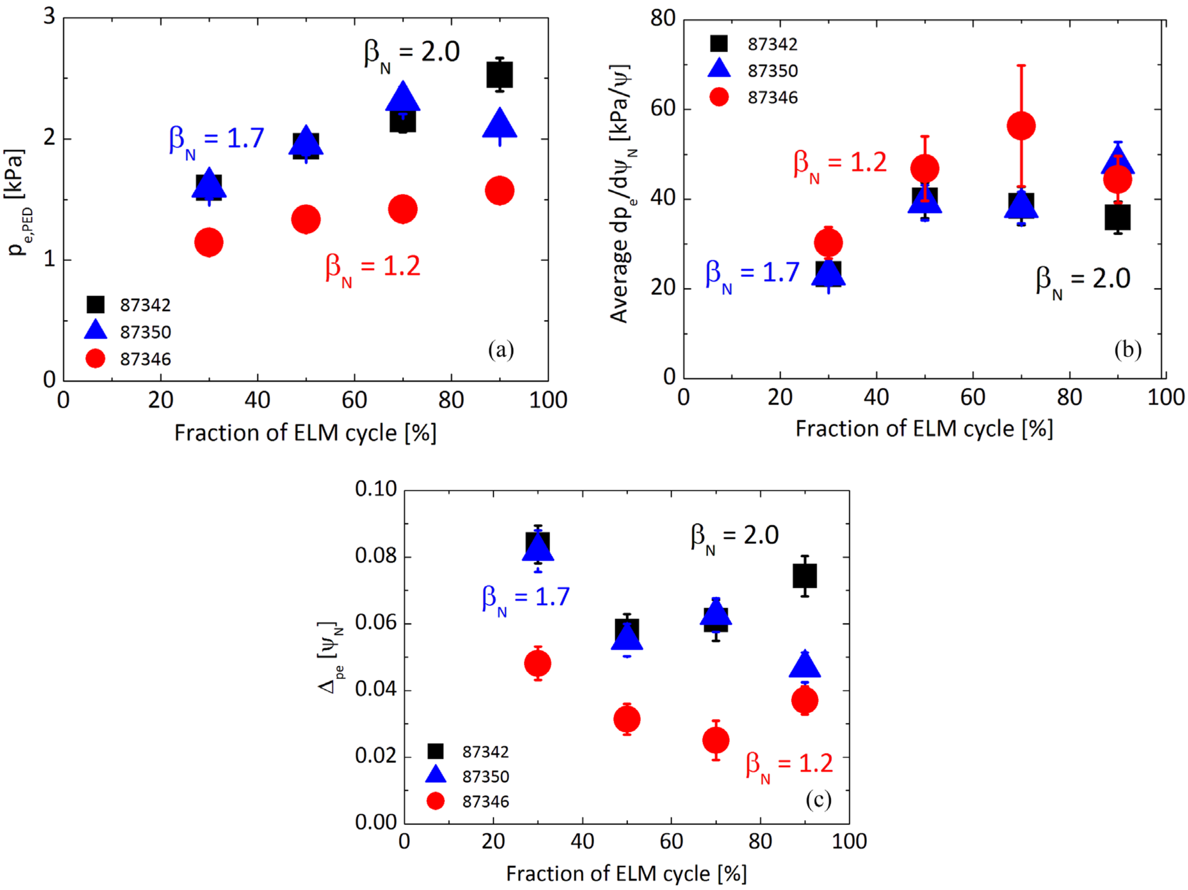

Figure 14. Pedestal p_e evolution during the type I ELM cycle for three H-modes of the 1.4 MA/1.7 T power scans at high D_2 gas injection: (*a*) $p_{e,PED}$, (*b*) average ∇p_e and (*c*) Δp_e as a function of normalized ELM fraction.

Table 1. Overview of the main plasma parameters of H-modes at low versus high I_p. All parameters are averaged in the steady time window Δt. $T_{e,PED}$ and $n_{e,PED}$ are pre-ELM values.

Pulse #	I_P (MA)	B_T (*T*)	Δt (s)	I_{loss} (MW)	P_{sep}/P_{L-H}	β_N	H_{98}	$T_{e,PED}$ (keV)	$n_{e,PED}$ (10^{19} m^{-3})
92432	3.0	2.8	8.7–9.7	33.0	2.2	2.15	1.0	1.10	5.86
84791	1.4	1.7	4.7–6.4	8.5	4.5	1.88	1.0	0.55	3.2
84794	1.4	1.7	5.0–6.0	15.6	8.5	2.74	1.1	0.93	2.56

of the best performing H-mode of the 1.4 MA power scans (#84794). It is interesting to note, though, that in the low I_p power scan at low gas injection an almost two-fold increase in pre-ELM $T_{e,PED}$, from 0.55 keV to 0.93 keV, is obtained when P_{sep} is greatly raised above P_{L-H}, from $P_{sep}/P_{L-H} = 4.5$ for #84791 to 8.5 for #84794 by increasing the auxiliary heating with neutral beam injection (see table 1 and [1]). On the other hand, in the high current H-mode $P_{sep}/P_{L-H} = 2.2$, since the higher B_T and plasma density raise P_{L-H}. In addition, a D_2 gas puff level of 1.8×10^{22} e s^{-1} is required in order to ensure W control and steady conditions (together with 4.5 MW central ICRH heating). The experiments could thus suggest that a significantly larger P_{sep}/P_{L-H} would be required to raise $T_{e,PED}$ substantially above the ~1 keV value observed in experiment, e.g. by further increasing the auxiliary heating and/or reducing the injected gas rate while still maintaining core W control. This hypothesis is currently under investigation with modelling activities and will be reported elsewhere.

The inter-ELM evolution of pedestal widths and gradients at low versus high plasma current is compared in figures 15–17. The pedestal top density increases monotonically during the ELM cycle both at low and high I_P, but the density drop after the ELM crash is larger in the discharge at low I_P and high P_{sep}/P_{L-H}. While the pedestal density widths are of similar magnitude at low and high I_P, the averaged pedestal density gradient is three times steeper at high than low I_P. At high current the density rebuilds inter-ELM initially through steepening of the gradient and narrowing of the width, while in the second half of the ELM cycle Δn_e and average gradient remain roughly constant within error bars. In contrast, at low I_P the density pedestal builds up via continuous steepening of the averaged gradient and narrowing of the width. $T_{e,PED}$ increases monotonically inter-ELM at high I_P, except for possibly saturating in the last 30% of the ELM cycle. The pedestal width and gradient temporal evolution are similar at low and high I_P, but ΔT_e is broader in the low I_P case,

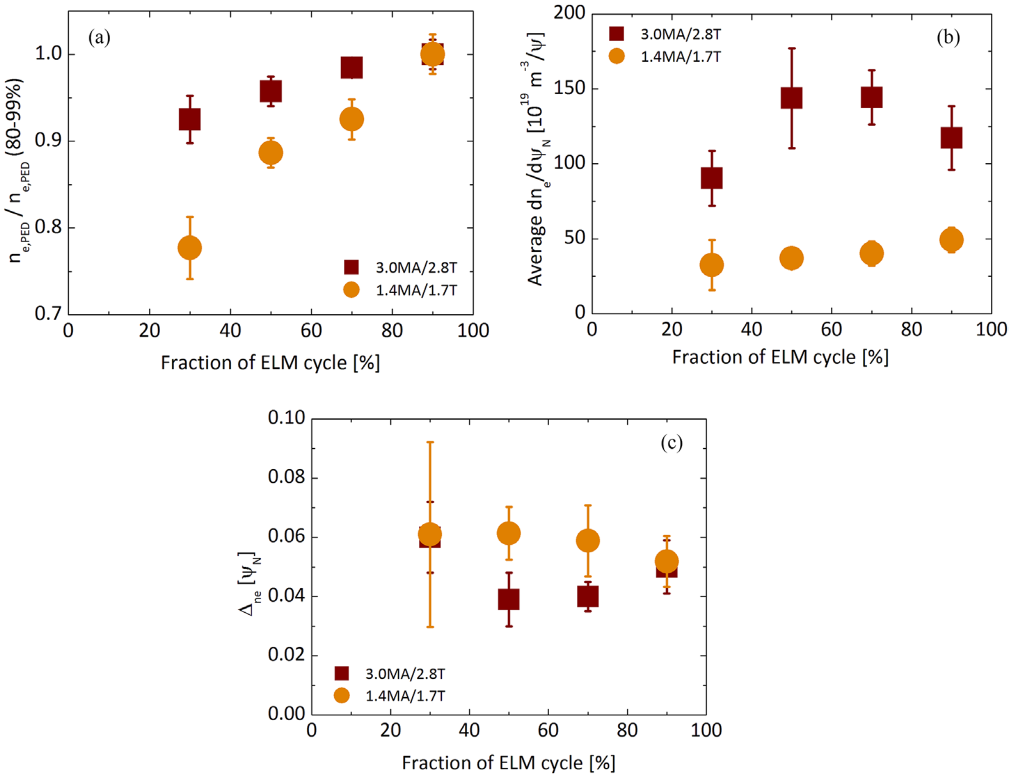

Figure 15. Pedestal density evolution during the type I ELM cycle at 1.4 MA/1.7 T and 3.0 MA/2.8 T: (*a*) $n_{\mathrm{e,PED}}$ normalized to the pre-ELM value (*b*) average ∇n_{e} and (*c*) Δn_{e} as a function of normalized ELM fraction.

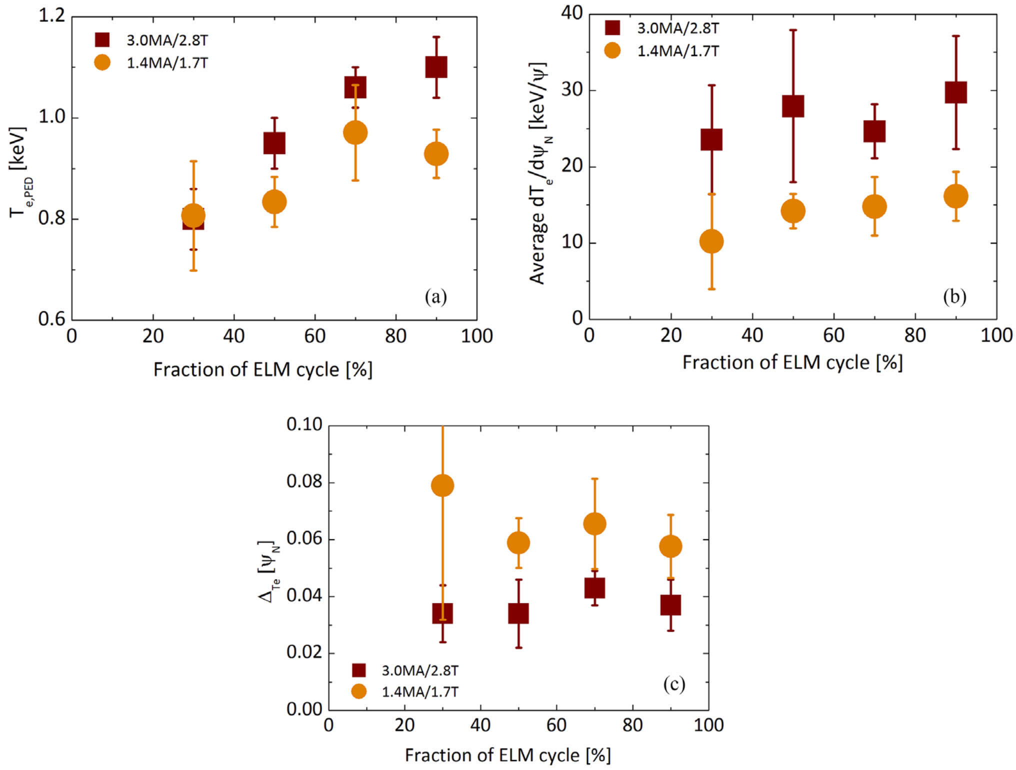

Figure 16. Pedestal T_{e} evolution during the type I ELM cycle at 1.4 MA/1.7 T and 3.0 MA/2.8 T: (*a*) $T_{\mathrm{e,PED}}$, (*b*) average ∇T_{e} and (*c*) ΔT_{e} as a function of normalized ELM fraction.

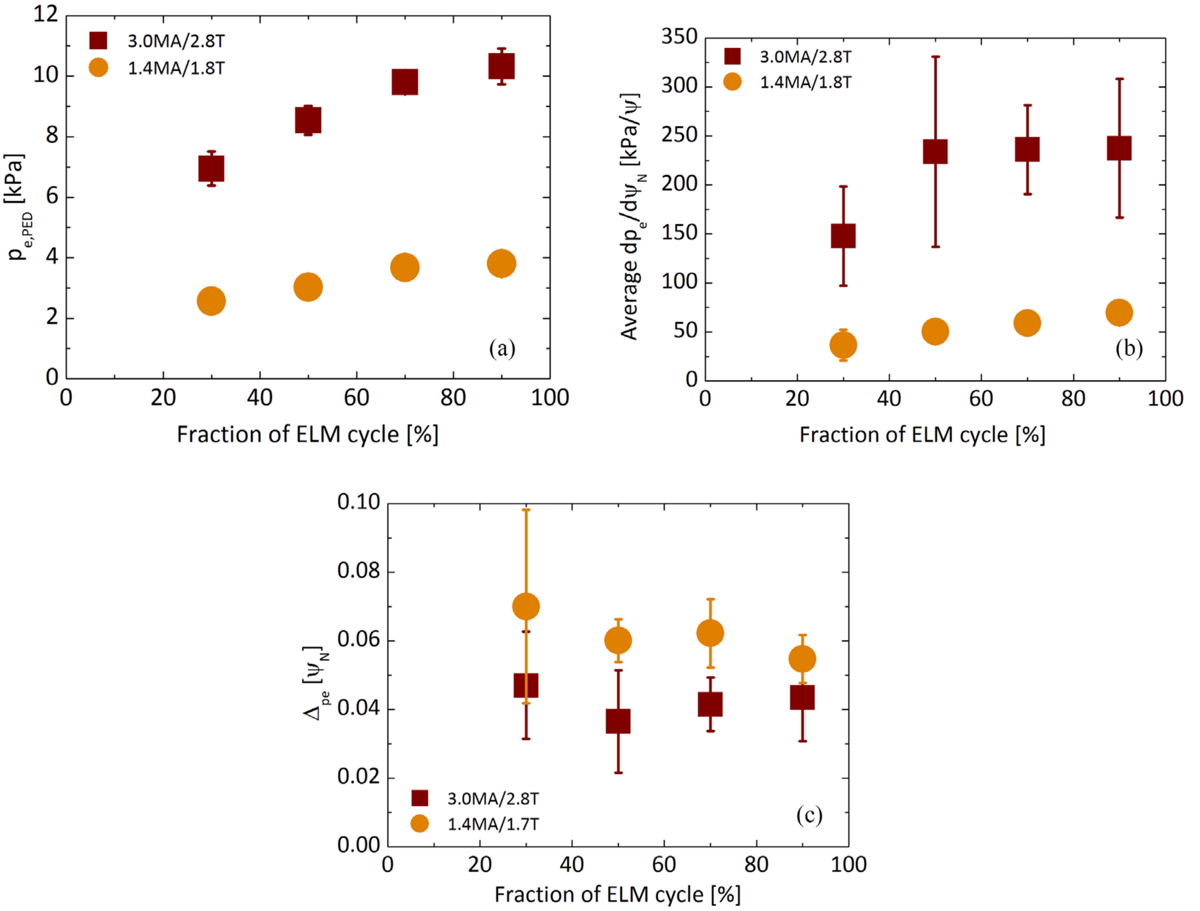

Figure 17. Inter-ELM temporal evolution of electron pedestal pressure at 1.4 MA/1.7 T and 3.0 MA/2.8 T: (*a*) $p_{\rm e,PED}$, (*b*) average $\nabla p_{\rm e}$ and (*c*) $\Delta p_{\rm e}$ as a function of normalized ELM fraction.

presumably due to the higher $P_{\rm sep}/P_{\rm L-H}$ ratio. On the other hand, the high $I_{\rm P}$ pedestal sustains a larger average temperature gradient.

In the high current H-mode, $p_{\rm e,PED}$ increases continuously inter-ELM until the ELM crash, with the average pedestal pressure gradient initially increasing and then saturating half way through the ELM cycle and with $\Delta p_{\rm e}$ roughly constant through the ELM cycle. The trends suggested by the data thus show dynamical behaviour consistent with the KBM constraint, which should however be confirmed or disproved by future edge gyrokinetic simulations and comparison to fluctuation levels measured by reflectometry. The linear MHD edge stability of the 3 MA discharge has been analysed with HELENA/MISHKA [34] with input the measured pre-ELM $n_{\rm e}$ and $T_{\rm e}$ profiles and using the Sauter formula [16, 17] to calculate the contribution of the bootstrap current to the total edge current. $T_{\rm i} = T_{\rm e}$ is assumed (consistent with charge exchange measurements) and the line averaged $Z_{\rm eff}$ from visible Bremsstrahlung is used in the calculation of the main ion density (with Be the main intrinsic impurity). The pedestal stability analysis is illustrated in the j-α diagram of figure 18, where the dashed black line represents the *P–B* stability boundary and the integers indicate the numbers of the most unstable n-modes. The operational point (magenta star) is close to the *P–B* boundary, indicating broad consistency with the *P–B* constraint. Since both *P–B* constraint and KBM constraint appear to be satisfied on the basis of our analysis, we conclude that the inter-ELM evolution of the 3 MA H-mode pedestal (#92432) is in agreement with the EPED assumptions.

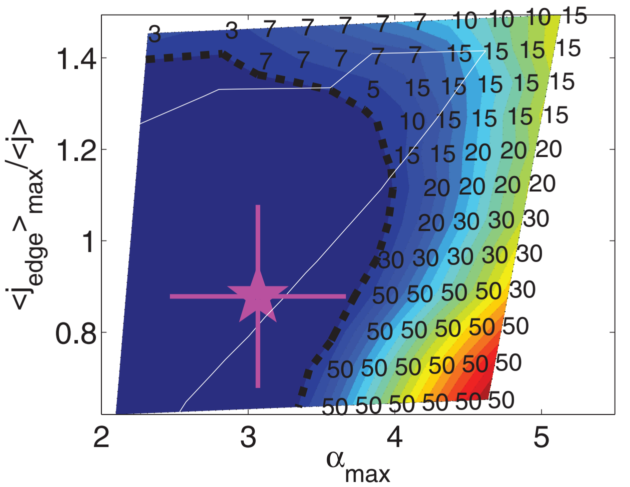

Figure 18. j-α edge stability diagram calculated with HELENA/MISHKA for the 3 MA pulse #92432. The dashed black line represents the *P–B* stability boundary, the thin white line the $n = \infty$ ideal MHD ballooning limit and the integers the values of the most unstable n-modes. The operational point (magenta star) is close to the *P–B* stability boundary.

5. Discussion and conclusions

The pedestal structure of type I ELMy H-modes has been analysed for JET-ILW. The electron pressure pedestal width is independent of ρ^* and increases proportionally to $\sqrt{\beta_{\text{pol,PED}}}$. Additional broadening of the pressure width is observed, at constant $\beta_{\text{pol,PED}}$, with increasing ν^* and/or neutral gas injection and the contribution of atomic physics effects in setting the width cannot as yet be ruled out. Neutral penetration alone does not appear to determine the shape of the edge density profile in JET-ILW and the pedestal electron density width is largely insensitive to variations in injected D_2 gas rate, except possibly at the highest power levels. The pedestal electron temperature width, on the other hand, broadens (and ∇T_{e} decreases) with D_2 gas rate at high power levels above $P_{\text{L–H}}$. Analysis of the ratio of density to temperature scale lengths in the JET-ILW edge transport barrier, $\eta_{\text{e}} = L_{n_{\text{e}}}/L_{T_{\text{e}}}$, derived from the experimental profiles without *mtanh* fit regularization, identifies η_{e} values of order 2–3 within experimental uncertainties, although HRTS data with higher spatial and temporal resolution are needed to enable a more accurate quantitative discrimination of η_{e}.

The paper extends existing understanding, represented in the stationary ELITE linear peeling–ballooning mode stability and the EPED pedestal structure models, to the dynamic evolution between ELM crashes in JET-ILW, in order to test the assumptions underlying these two models. Study of the inter-ELM pedestal evolution in a range of JET-ILW H-modes with varying plasma conditions shows that avoiding saturation of the temperature gradient as the pedestal rebuilds in between ELM crashes is crucial to maximizing pedestal performance. The inter-ELM pedestal evolution in JET-ILW doesn’t follow one single dynamic pattern, but varies depending on plasma operation conditions, such as auxiliary heating and/or gas injection levels, and is not always consistent with the assumptions underpinning the EPED model. In particular, the inter-ELM pedestal pressure evolution at high β_{N} and high gas injection appears to be inconsistent with the EPED model assumptions, despite qualitative consistency with the KBM constraint, since the *P–B* constraint is not satisfied.

Recent non-linear GENE simulations of a sample JET-ILW pedestal at high D_2 gas rate indicate that MTM and electron temperature gradient turbulence, together with neoclassical transport, is consistent with power balance across the pedestal, with KBMs largely insignificant over the edge transport barrier, except very near the LCFS [32]. As MTMs are driven by the electron temperature gradient, they exhibit the characteristics of a mode that clamps the T_{e} pedestal evolution, and could therefore be the dominant turbulence in the JET-ILW pedestal as the D_2 gas rate is progressively increased at given input power.

Edge gyrokinetic analyses and experimental characterization of the turbulence driving the residual pedestal transport inter-ELM are needed in order to advance understanding of the physics at play in JET-ILW pedestals and gain confidence in predictions for ITER and beyond.

Acknowledgments

This work has been carried out within the framework of the EUROfusion Consortium and has received funding from the Euratom research and training programme 2014–2018 under grant agreement No 633053. The views and opinions expressed herein do not necessarily reflect those of the European Commission.

ORCID iDs

H. Wilson https://orcid.org/0000-0003-3333-7470
J. Flanagan https://orcid.org/0000-0003-4179-9616

References

[1] Maggi C.F. *et al* 2015 *Nucl. Fusion* **55** 113031
[2] Maggi C.F. *et al* 2014 *Nucl. Fusion* **54** 023007
[3] Challis C. *et al* 2015 *Nucl. Fusion* **55** 053031
[4] Groebner R.J. *et al* 2002 *Phys. Plasmas* **9** 2134
[5] Snyder P.B. *et al* 2009 *Phys. Plasmas* **16** 056118
[6] Pasqualotto R. *et al* 2004 *Rev. Sci. Instrum.* **75** 3891
[7] De la Luna E. *et al* 2004 *Rev. Sci. Instrum.* **75** 3831
[8] Brix M. *et al* 2012 *Rev. Sci. Instrum.* **83** 10D533
[9] Sirinelli A. *et al* 2010 *Rev. Sci. Instrum.* **81** 10D939
[10] Groebner R.G. *et al* 1998 *Phys. Plasmas* **5** 1800
[11] Frassinetti L., *et al* 2012 *Rev. Sci. Instrum.* **83** 013506
[12] Leyland M. *et al* 2016 *Rev Sci. Instrum.* **87** 013507
[13] Kallenbach A. *et al* 2005 *J. Nucl. Mater.* **337–9** 381
[14] Stefanikova E. *et al* 2016 *43rd EPS Conf. on Plasma Physics (Leuven, Belgium, 4–8 July 2016)*
[15] Dunne M. *et al* 2017 *Plasma Phys. Control. Fusion* **59** 014017
[16] Sauter O. *et al* 1999 *Phys. Plasmas* **6** 2834
[17] Sauter O. *et al* 2002 *Phys. Plasmas* **9** 5140
[18] Belli E. and Candy J. 2008 *Plasma Phys. Control. Fusion* **50** 095010
[19] Belli E. and Candy J. 2012 *Plasma Phys. Control. Fusion* **54** 015015
[20] Horvath L. *et al* 2016 *43rd EPS Conf. on Plasma Physics (Leuven, Belgium, 4–8 July 2016)*
[21] Frassinetti L. *et al* 2017 *Plasma Phys. Control. Fusion* **59** 014014
[22] Beurskens M.N.A. *et al* 2011 *Phys. Plasmas* **18** 056120
[23] Urano H. *et al* 2008 *Nucl. Fusion* **48** 045008
[24] Chapman I.T. *et al* 2016 Joint experiments tailoring the plasma evolution to maximise pedestal performance *Preprint: 2016 IAEA Fusion Energy Conf. (Kyoto, Japan, 17–22 October 2016)* p EX/3–6 (https://nucleus.iaea.org/sites/fusionportal/Pages/Fusion%20Energy%20Conference.aspx)
[25] Urano H. *et al* 2016 Global stabilization effect of Shafranov shift on the edge pedestal plasmas in JET and JT-60U *Preprint: 2016 IAEA Fusion Energy Conf. (Kyoto, Japan, 17–22 October 2016)* p EX/3–4 (https://nucleus.iaea.org/sites/fusionportal/Pages/Fusion%20Energy%20Conference.aspx)
[26] Leyland M. *et al* 2015 *Nucl. Fusion* **55** 013019
[27] Frassinetti L. *et al* 2017 *Nucl. Fusion* **57** 016012
[28] Horton L.D. *et al* 2005 *Nucl. Fusion* **45** 856
[29] Saarelma S. *et al* 2013 *Nucl. Fusion* **53** 123012
[30] Wilson H.R. *et al* 2002 *Phys. Plasmas* **9** 1277
[31] Snyder P.B. *et al* 2002 *Phys. Plasmas* **9** 2037
[32] Hatch D.R. *et al* 2016 *Nucl. Fusion* **56** 104003
[33] ITER Physics Basis (ed) *et al* 1999 *Nucl. Fusion* **39** 2137
[34] Mikhailovskii A.B. *et al* 1997 *Plasma Phys. Rep.* **23** 844